

Lightning black holes as unidentified TeV sources

Kouichi Hirotani, Hung-Yi Pu · Satoki Matsushita

Received: date / Accepted: date

Abstract Imaging Atmospheric Cherenkov Telescopes have revealed more than 100 TeV sources along the Galactic Plane, around 45% of them remain unidentified. However, radio observations revealed that dense molecular clumps are associated with 67% of 18 unidentified TeV sources. In this paper, we propose that an electron-positron magnetospheric accelerator emits detectable TeV gamma-rays when a rapidly rotating black hole enters a gaseous cloud. Since the general-relativistic effect plays an essential role in this magnetospheric lepton accelerator scenario, the emissions take place in the direct vicinity of the event horizon, resulting in a point-like gamma-ray image. We demonstrate that their gamma-ray spectra have two peaks around 0.1 GeV and 0.1 TeV and that the accelerators become most luminous when the mass accretion rate becomes about 0.01% of the Eddington accretion rate. We compare the results with alternative scenarios such as the cosmic-ray hadron scenario, which predicts an extended morphology of the gamma-ray image with a single power-law photon spectrum from GeV to 100 TeV.

Keywords Black hole physics · Gamma-rays · Magnetic fields

1 Introduction

The Imaging Atmospheric Cherenkov Telescopes (IACTs) provides a wealth of new data on various energetic astrophysical objects, increasing the number

Kouichi Hirotani and Satoki Matsushita
11F of AS/NTU Astronomy-Mathematics Building, No.1, Sec. 4, Roosevelt Rd, Taipei 10617, Taiwan, R.O.C.
Tel.: +886-2-2366-5406
Fax: +886-2-2367-7849
E-mail: hirotani@asiaa.sinica.edu.tw

Hung-Yi Pu
Perimeter Institute for Theoretical Physics, 31 Caroline Street North, Waterloo, ON, N2L 2Y5, Canada

of detected very-high-energy (VHE) gamma-ray sources, typically between 0.01 and 100 TeV, from 7 to more than 200 in this century ¹. Among the presently operating three IACTs, High Energy Stereoscopic System (HESS) [Wilhelmi (2009)] has so far discovered 42 new VHE sources along the Galactic Plane, 22 of which are still unidentified. The nature of these unidentified VHE sources may be hadronic origin [Black & Fazio (1973), Issa & Wolfendale (1981)], because protons can be efficiently accelerated into VHE in a supernova remnant to penetrate into adjacent dense molecular clouds, which leads to an extended gamma-ray image. By a systematic comparison between the published HESS data and the molecular radio line data, 38 sources are found to be associated with dense molecular clumps out of the 49 Galactic VHE sources covered by 12 mm observations [de Wilt et al. (2017)].

There is, however, an alternative scenario for the VHE emissions from gaseous clouds. In the Milky Way, molecular gas is mostly located in giant molecular clouds, in which massive stars are occasionally formed. If a massive star evolves into a black hole and encounters an adjacent molecular clouds, it accretes gases. It is, therefore, noteworthy that a rapidly rotating, stellar-mass black hole emits copious gamma-rays in 0.001-1 TeV [Hirotani & Pu (2016b)], provided that its dimensionless accretion rate $\dot{m} \equiv \dot{M}/\dot{M}_{\text{Edd}}$, satisfies $6 \times 10^{-5} < \dot{m} < 2 \times 10^{-4}$, where \dot{M} designates the mass accretion rate, $\dot{M}_{\text{Edd}} \equiv 1.39 \times 10^{19} M_1 \text{g s}^{-1}$ is the Eddington accretion rate, $M_1 = M/(10M_\odot)$ and M_\odot denotes the solar mass. The electric currents flowing in such an accreting plasma create the magnetic field threading the event horizon. In this leptonic scenario, migratory electrons and positrons (e^\pm s) are accelerated to TeV by a strong electric field exerted along these magnetic field lines, and cascade into many pairs as a result of the collisions between the VHE photons emitted by the gap-accelerated e^\pm s and the IR photons emitted by the hot e^- 's in the equatorial accretion flow. The resulting gamma radiation takes place only near the black hole; thus, their VHE image should have a point-like morphology with a spectral turnover around TeV.

2 Black hole accretion in a gaseous cloud

When a black hole moves in a gaseous cloud, the particles are captured by the hole's gravity to form an accretion flow. Since the temperature is very low in a molecular cloud, the black hole will move with a supersonic velocity V , forming a bow shock behind. Under this situation, the gas pressure can be neglected and the particles within the impact parameter $r_B \sim GMV^{-2}$ from the black hole will be captured. For a homogeneous gas, the mass accretion rate becomes [Bondi & Hoyle (1944)] $\dot{M}_B = 4\pi\lambda(GM)^2(C_S^2 + V^2)^{-3/2}\rho \approx 4\pi\lambda(GM)^2V^{-3}\rho$, where ρ denotes the mass density of the gas, λ a constant of order unity, G the gravitational constant, and C_S the sound speed in the homogeneous gas; the last near equality comes from the supersonic nature (i.e., $V \gg C_S$) of

¹ TeV Catalog (<http://www.tevcat.uchicago.edu>)

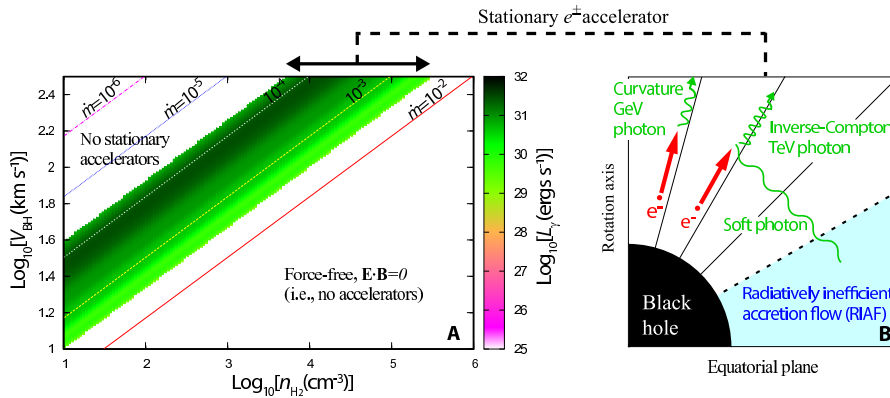


Fig. 1 (A) Luminosity of black-hole lepton accelerators when a ten-solar-mass, extremely rotating ($a = 0.99r_g$) black hole is moving with velocity V in a cloud with molecule hydrogen density n_{H_2} . For an atomic hydrogen gas with density n_{HI} , put $n_{\text{H}_2} = n_{\text{HI}}/2$, because the mass is halved. The five straight lines correspond to the Bondi-Hoyle accretion rates, 10^{-2} , 10^{-3} , 10^{-4} , 10^{-5} , and 10^{-6} , as labeled. In the lower-right white region, the enhanced photon illumination from the equatorial accretion flow results in an efficient pair production, and hence a complete screening of the magnetic-field-aligned electric field; thus, the accelerator vanishes in this region. In the upper-left white region, stationary accelerators cannot be formed (see text). Thus, stationary accelerators arise only in the green-black region. (B) Schematic figure (side view) of a black-hole magnetosphere. The polar funnel is assumed to be bounded from the radiatively inefficient accretion flow (cyan region) at colatitude $\theta = 60^\circ$ (dashed line) from the rotation axis (ordinate).

accretion. For a molecular hydrogen gas, we obtain the dimensionless Bondi accretion rate $\dot{m}_B \equiv \dot{M}_B/\dot{M}_{\text{Edd}} = 5.4 \times 10^{-9} \lambda n_{\text{H}_2} M_1 (V/10^2 \text{ km s}^{-1})^{-3}$, where n_{H_2} denotes the number density of hydrogen molecules per cm^3 . Representative values of \dot{m}_B are plotted as the five straight lines in figure 1A.

Since the accreting gases have little angular momentum as a whole with respect to the black hole, they form an accretion disk only within a radius that is much less than r_B . Thus, we neglect the mass loss as a disk wind between r_B and the inner-most region, and evaluate the accretion rate near the black hole, \dot{m} , with \dot{m}_B . In what follows, we consider a ten solar mass black hole, which is typical as a stellar-mass black hole [Tetarenko et al. (2016), Corral-Santana et al. (2016)]. It is reasonable to suppose that such black holes have kick velocities of $V < 10^2 \text{ km s}^{-1}$ with respect to the star-forming region. Under this circumstance, a typical velocity dispersion in a molecular cloud, $\Delta V < 10 \text{ km s}^{-1}$, is an order of magnitude less than V . Accordingly, the net specific angular momentum of the gas at r_B , which is typically $r_B \Delta V$, is much less than the Keplerian value, $r_B V = \sqrt{GM r_B}$. At a much smaller radius $r = (\Delta V/V)^2 r_B < 0.01 r_B$, $r_B \Delta V$ equals the Keplerian value; therefore, a disk is formed within this radius. Since the accreting gas does not have to lose angular momentum when falling from $r = r_B$ to $(\Delta V/V)^2 r_B$, we neglect the mass loss in this region and evaluate the accretion rate \dot{m} near the BH with the Bondi-Hoyle accretion rate \dot{m}_B for simplicity in the present paper.

3 Development of charge-starved magnetosphere

When \dot{m} becomes typically less than 10^{-2} , Coulomb collisions become so inefficient that the accreting protons thermal energy cannot be efficiently transferred to the electrons. If the accretion rate decreases to $\dot{m} < 10^{-2.5}$, such a radiatively inefficient accretion flow (RIAF) [Ichimaru (1979), Narayan (1994), Mahadevan (1997)] cannot supply enough soft gamma-rays that are needed to sustain the magnetosphere force-free [Levinson (2011)]. Accordingly, a charge-starved, nearly vacuum magnetosphere develops in the polar funnel (fig. 1B), because the equatorial accreting plasmas cannot penetrate there due to the centrifugal-force barrier. If the accretion rate further decreases to $\dot{m} < 6 \times 10^{-5}$, stationary pair production cascade cannot be sustained. However, the luminosity of such a non-stationary accelerator becomes less than the stationary cases, because only a weaker magnetic field can be confined near the black hole for a lower accretion rate. Thus, we consider only the range $6 \times 10^{-5} < \dot{m} < 2 \times 10^{-4}$ (green-black region in fig. 1A) and concentrate on stationary accelerators. It is noteworthy that if a stellar-mass black hole moves slowly (i.e., $V \ll 10^2 \text{ km s}^{-1}$), its accelerator can be activated with a low gas density (e.g., $n_{\text{H}_2} \ll 10^3 \text{ cm}^{-3}$; fig. 1A). Thus, a significant gamma-ray emission is possible when a black hole encounters not only a dense molecular cloud but also a diffuse molecular gas or even an atomic gas.

4 Lepton accelerator in black hole magnetospheres

In a vacuum magnetosphere, an electric field, E_{\parallel} , arises along the magnetic field lines. Accordingly, electrons and positrons (red arrows in fig. 1B) are accelerated into ultra-relativistic energies to emit high-energy gamma-rays (wavy line with middle wavelength) via the curvature process (a kind of the synchrotron process whose the electron's gyro radius is replaced with the macroscopic curvature radius of three-dimensional electron's motion) and VHE gamma-rays (wavy line with shortest wavelength) via the inverse-Compton (IC) scatterings of the soft photons (wavy line with longest wavelength) emitted from the RIAF. A fraction of such VHE photons collide with the soft RIAF photons to materialize as e^{\pm} pairs, which partially screen the original E_{\parallel} when they separate. It is noteworthy that pair annihilation is negligible compared to pair production in BH gaps. To compute the actual strength of E_{\parallel} , we solve the e^{\pm} pair production cascade in a stationary and axisymmetric magnetosphere on the meridional plane (r, θ), where r denotes the Boyer-Lindquist radial coordinate, and θ does the colatitude measured from the rotation axis. The black holes rotational energy is electromagnetically extracted via the Blandford-Znajek process [Blandford & Znajek (1977)] and partially dissipated as particle acceleration and the resultant radiation within the accelerator. It is noteworthy that the electrodynamics of this lepton accelerator is essentially described by the general-relativistic Goldreich-Julian charge density, which is governed by the magnetic-field strength and the frame-dragging

effects. Thus, the accelerator solution little depends on the magnetic field configuration near the event horizon. We therefore assume that the magnetic field is radial in the meridional plane and that magnetic axis is aligned with the rotation axis. The magnetic field lines are twisted in the azimuthal direction due to the frame-dragging effect, and its curvature radius is assumed to be r_g in the local reference frame. This assumption modestly affects the curvature spectrum, but does not affect the entire electrodynamics, because the pair-production process, and hence the screening of E_{\parallel} is governed by the highest-energy, IC-scattered photons.

5 Basic equations

Let us quantify the accelerator electrodynamics. In a rotating black-hole magnetosphere, electron-positron accelerator is formed in the direct vicinity of the event horizon. Thus, we start with describing the background spacetime in a fully general-relativistic way. We adopt the geometrized unit, putting $c = G = 1$, where c and G denote the speed of light and the gravitational constant, respectively. Around a rotating BH, the spacetime geometry is described by the Kerr metric [Kerr (1963)]. In the Boyer-Lindquist coordinates, it becomes [Boyer & Lindquist (1967)]

$$ds^2 = g_{tt}dt^2 + 2g_{t\varphi}dtd\varphi + g_{\varphi\varphi}d\varphi^2 + g_{rr}dr^2 + g_{\theta\theta}d\theta^2, \quad (1)$$

where

$$g_{tt} \equiv -\frac{\Delta - a^2 \sin^2 \theta}{\Sigma}, \quad g_{t\varphi} \equiv -\frac{2Mar \sin^2 \theta}{\Sigma}, \quad (2)$$

$$g_{\varphi\varphi} \equiv \frac{A \sin^2 \theta}{\Sigma}, \quad g_{rr} \equiv \frac{\Sigma}{\Delta}, \quad g_{\theta\theta} \equiv \Sigma; \quad (3)$$

$\Delta \equiv r^2 - 2Mr + a^2$, $\Sigma \equiv r^2 + a^2 \cos^2 \theta$, $A \equiv (r^2 + a^2)^2 - \Delta a^2 \sin^2 \theta$. At the horizon, we obtain $\Delta = 0$, which gives the horizon radius, $r_H \equiv M + \sqrt{M^2 - a^2}$, where M corresponds to the gravitational radius, $r_g \equiv GMc^{-2} = M$. The spin parameter a becomes $a = M$ for a maximally rotating BH, and becomes $a = 0$ for a non-rotating BH. The spacetime dragging frequency is given by $\omega(r, \theta) = -g_{t\varphi}/g_{\varphi\varphi}$, which decreases outwards as $\omega \propto r^{-3}$ at $r \gg r_g = M$.

We assume that the non-corotational potential Φ depends on t and φ only through the form $\varphi - \Omega_F t$, and put

$$F_{\mu t} + \Omega_F F_{\mu\varphi} = -\partial_{\mu}\Phi(r, \theta, \varphi - \Omega_F t), \quad (4)$$

where Ω_F denotes the magnetic-field-line rotational angular frequency. We refer to such a solution as a ‘stationary’ solution in the present paper.

The Gauss’s law gives the Poisson equation that describes Φ in a three dimensional magnetosphere [Hirotani (2006)],

$$-\frac{1}{\sqrt{-g}}\partial_{\mu}\left(\frac{\sqrt{-g}}{\rho_w^2}g^{\mu\nu}g_{\varphi\varphi}\partial_{\nu}\Phi\right) = 4\pi(\rho - \rho_{GJ}), \quad (5)$$

where $\rho_w^2 \equiv g_{t\varphi}^2 - g_{tt}g_{\varphi\varphi} = \Delta \sin^2 \theta$, and the general-relativistic Goldreich-Julian (GJ) charge density is defined as [Hirotani (2006)]

$$\rho_{\text{GJ}} \equiv \frac{1}{4\pi\sqrt{-g}} \partial_\mu \left[\frac{\sqrt{-g}}{\rho_w^2} g^{\mu\nu} g_{\varphi\varphi} (\Omega_{\text{F}} - \omega) F_{\varphi\nu} \right]. \quad (6)$$

Far away from the horizon, $r \gg M$, equation (6) reduces to the ordinary, special-relativistic expression of the GJ charge density [Goldreich & Julian (1969), Mestel (1971)],

$$\rho_{\text{GJ}} \equiv -\frac{\boldsymbol{\Omega} \cdot \mathbf{B}}{2\pi c} + \frac{(\boldsymbol{\Omega} \times \mathbf{r}) \cdot (\nabla \times \mathbf{B})}{4\pi c}. \quad (7)$$

Therefore, the corrections due to magnetospheric currents, which are expressed by the second term of eq. (7), are included in equation (6).

If the real charge density ρ deviates from the rotationally induced Goldreich-Julian charge density, ρ_{GJ} , in some region, equation (5) shows that Φ changes as a function of position. Thus, an acceleration electric field, $E_{\parallel} = -\partial\Phi/\partial s$, arises along the magnetic field line, where s denotes the distance along the magnetic field line. A gap is defined as the spatial region in which E_{\parallel} is non-vanishing. At the null charge surface, ρ_{GJ} changes sign by definition. Thus, a vacuum gap, in which $|\rho| \ll |\rho_{\text{GJ}}|$, appears around the null-charge surface, because $\partial E_{\parallel}/\partial s$ should have opposite signs at the inner and outer boundaries [Cheng et al. (1986a), Ciang & Romani (1992), Romani (1996), Cheng et al. (2001)]. As an extension of the vacuum gap, a non-vacuum gap, in which $|\rho|$ becomes a good fraction of $|\rho_{\text{GJ}}|$, also appears around the null-charge surface (§ 2.3.2 of HP 16), unless the injected current across either the inner or the outer boundary becomes a substantial fraction of the GJ value.

In previous series of our papers, e.g., [Hirotani et al. (2016a)], we have assumed $\Delta \ll M^2$ in Equation (5), expanding the left-hand side in the series of Δ/M^2 and pick up only the leading orders. However, in the present report, we discard this approximation, and consider all the terms that arise at $\Delta \sim M^2$ or $\Delta \gg M^2$.

It should be noted that ρ_{GJ} vanishes, and hence the null surface appears near the place where Ω_{F} coincides with the space-time dragging angular frequency, ω [Beskin et al. (1992)]. The deviation of the null surface from this $\omega(r, \theta) = \Omega_{\text{F}}$ surface is, indeed, small, as figure 1 of [Hirotani & Okamoto (1998)] indicates. Since ω can match Ω_{F} only near the horizon, the null surface, and hence the gap generally appears within one or two gravitational radii above the horizon, irrespective of the BH mass.

6 Results

We apply the method to a stellar-mass black hole with mass $M = 10M_{\odot}$. To consider an efficient emission, we consider an extremely rotating black hole, $a = 0.99r_{\text{g}}$, because the accelerator luminosity rapidly increases as $a \rightarrow r_{\text{g}}$ (10). Owing to the frame-dragging effects, the Goldreich-Julian charge density decreases outwards around a rotating black hole. As a result, a negative E_{\parallel}

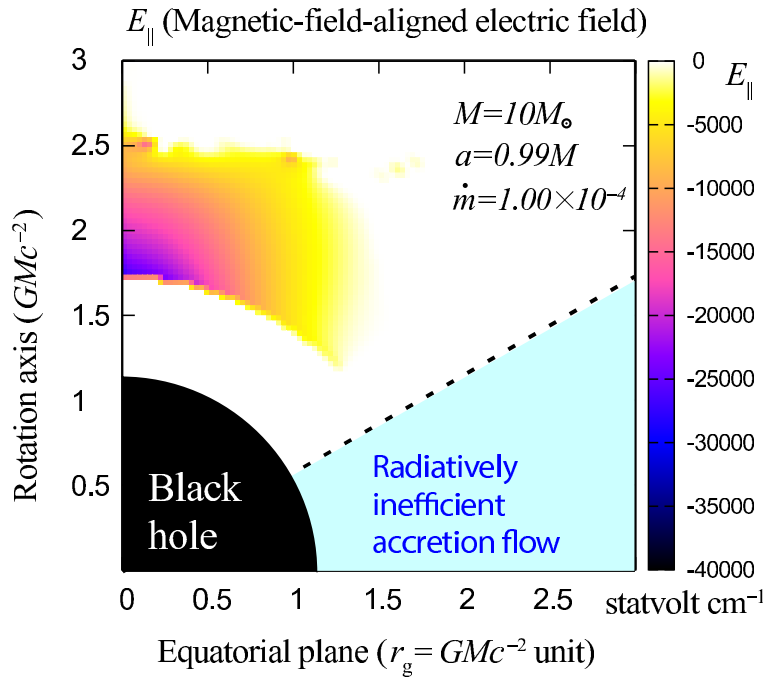


Fig. 2 Magnetic-field-aligned electric field, E_{\parallel} , on the meridional plane. The filled black circle on the bottom left corner shows a black hole rotating along the ordinate. The mass and the spin parameter of the black hole are $M = 10M_{\odot}$ and $a = 0.99r_g$. Both axes are normalized by the gravitational radius, $r_g = GMc^{-2}$. The lepton accelerator appears only in the polar funnel, $\theta < 60^\circ$. The dimensionless accretion rate is $\dot{m} = 10^{-4}$. Magnetic field is assumed to be radial on the meridional plane, and be rotating with angular frequency $\Omega_F = 0.5\omega_H$, where ω_H denotes the black holes spin angular frequency. The null-charge surface is located at radial coordinate, $r = 1.73r_g$, whose θ dependence is weak.

arises near the null-charge surface, which is located very close to the event horizon (fig. 2).

In fig. 3, we also plot $E_{\parallel}(r, \theta)$ at four discrete colatitudes, $\theta = 0^\circ, 15^\circ, 30^\circ$, and 45° . It follows that E_{\parallel} peaks slightly inside the null surface (vertical dashed line), and that it maximizes at $\theta = 0^\circ$ (i.e., along the rotation axis). The reason why E_{\parallel} maximizes along the rotation axis is that magnetic fluxes concentrate towards the rotation axis as the black hole spin approaches its maximum value (i.e., as $a \rightarrow r_g$) [Komissarov & McKinney (2007), Tchekhovskoy et al. (2010)]. Therefore, to consider the greatest gamma-ray flux, we focus on the emission along the rotation axis, $\theta = 0^\circ$. The acceleration electric field, E_{\parallel} , decreases slowly outside the null surface in the same way as pulsar outer gaps [Hirotani & Shibata (1999)]. This is because the two-dimensional screening effect of E_{\parallel} works when the gap longitudinal (i.e., radial) width becomes non-negligible compared to its trans-field (i.e., meridional) thickness.

The created e^{\pm} s are accelerated by the E_{\parallel} in opposite directions, emitting copious gamma-rays via the curvature process in $0.01 - 3$ GeV and via the

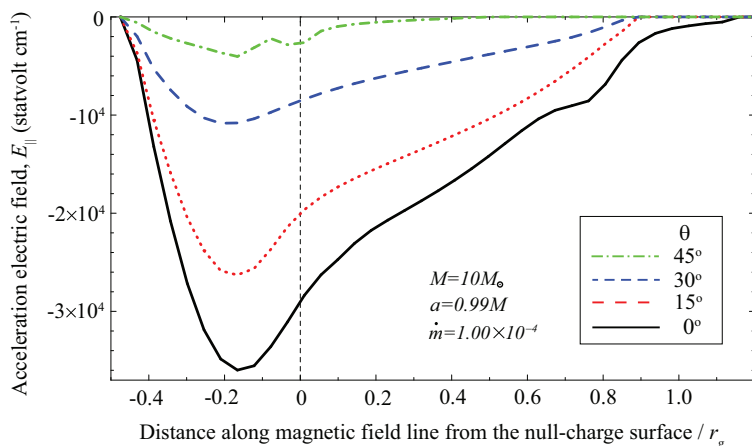


Fig. 3 Distribution of the magnetic-field-aligned electric field, E_{\parallel} , that is presented in figure 1, at four discrete colatitudes as labeled in the box, where $\theta = 0^\circ$ corresponds to the rotation axis. The abscissa denotes the distance along the magnetic field from the null-charge surface, where the general relativistic Goldreich-Julian charge density vanishes due to the spacetime dragging around a rotating black hole. Black hole’s mass ($M = 10M_{\odot}$), spin ($a = 0.99r_g$), and the accretion rate ($\dot{m} = 1.00 \times 10^{-4}$) are common with figure 1. The vertical dashed line shows the position of the null-charge surface along $\theta = 0^\circ$; however, its position little depends on θ because we assume $\Omega_F = 0.5\omega_H$ (see the main text).

IC process in 0.01 – 1 TeV (fig. 4). The characteristic photon energy in the curvature process is given by $h\nu_c = (3/2)\hbar c\gamma^3/\rho_c$, where h denotes the Planck constant and $\hbar \equiv h/2\pi$. At each place in the gap, electrons have Lorentz factors typically in the range $10^6 < \gamma < 3 \times 10^6$. To evaluate the curvature radius ρ_c , we assume that the horizon-threading magnetic field lines bend in the toroidal direction due to the frame dragging and adopt $\rho_c = r_g$. Since the pair production is sustained by the TeV photons (emitted via the IC process), the gap electrodynamics is little affected by the actual value of ρ_c , which appears only in the curvature process. Thus, we adopt this representative value, $\rho_c = r_g$. The IC photon energy is limited by the electron kinetic energy whose upper bound is about 1.5 TeV. Thus, the IC photons have typical energies between 0.01 TeV and 1 TeV.

It also follows from figure 4 that the gamma-ray luminosity increases with decreasing accretion rates. This is because the decreased RIAF soft photon field increases the pair-production mean-free path, the accelerator width along the magnetic field lines, and hence the electric potential drop. What is more, the emission becomes detectable with Fermi/LAT² and IACTs such as CTA³, if the distance is within 1 kpc, and if the dimensionless accretion rate resides in the narrow range, $6 \times 10^{-5} < \dot{m} < 2 \times 10^{-4}$. The gamma-ray spectrum exhibits a turnover around TeV, because electron Lorentz factors are limited below 1.6 TeV due to the curvature-radiation drag force. A caution should be

² LAT Performance (https://www.slac.stanford.edu/exp/glast/groups/canda/lat_Performance.htm)

³ CTA Performance (https://portal.cta-observatory.org/CTA_Observatory/performance/SitePages/Hom.aspx)

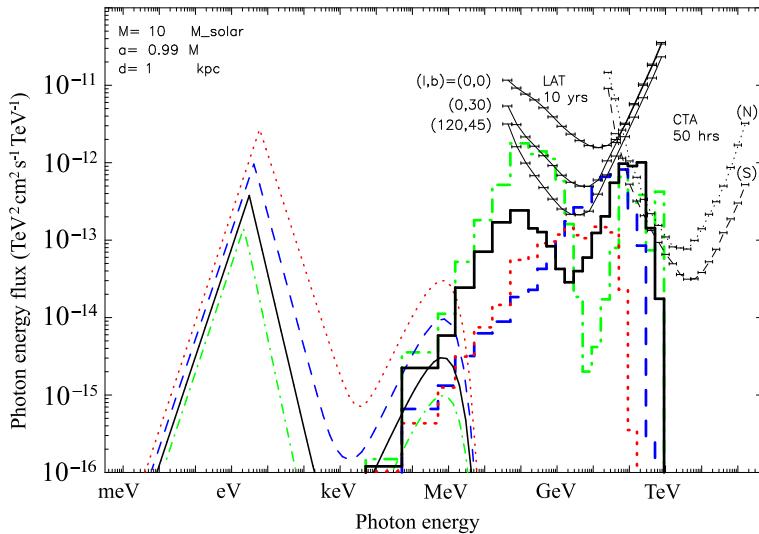


Fig. 4 Spectrum of a black-hole lepton accelerator. The black hole mass and spin are common with figure 1. The red dotted, blue dashed, black solid, and green dash-dotted curves correspond to the dimensionless accretion rate of $10^{-3.50}$, $10^{-3.75}$, 10^{-4} , and $10^{-4.25}$, respectively. The distance is assumed to be 1 kpc. The thin curves on the left denote the input spectra of the advection-dominated accretion flow, a kind of RIAF. Such soft photons illuminate the accelerator in the polar funnel. The thick lines denote the spectra of the gamma-rays emitted from the accelerator. The 0.1 – 10 GeV photons are emitted via the curvature process, while those in 0.01 – 1 TeV are via the inverse-Compton (IC) process. The detection limits of the Large Area Telescope (LAT) aboard the Fermi space observatory after ten-year observation are indicated by the thin solid curves. Also, the detection limits of the Cherenkov Telescope Array (CTA) after a 50-hour observation are shown by the thin dashed and dotted curves; (N) denotes the detection limit of the CTA in the northern-hemisphere, while (S) denotes those in the southern hemisphere.

made, however, on the assumption of a stationary electron-positron pair cascade. If the cascade takes place in a time-dependent manner as suggested with Particle-in-Cell simulations [Levinson & Segev (2017)], the spectra might appear different from the present stationary analysis. The present gap luminosity gives an estimate of the maximally possible luminosity of a gap, whose electrodynamic structure may be variable in time. The dependence of the solutions on the BH spin will be discussed in our subsequent paper [Hirota et al. (2018)].

Let us analytically examine why the gap luminosity maximizes when $\dot{m} \approx 10^{-4}$. At radius r , the soft photon number density, n_s , can be estimated as

$$n_s = \frac{L_s/c}{4\pi r^2 h\nu_s} = 1.3 \times 10^{20} M_1^{-2} \left(\frac{10r_g}{r} \frac{d}{10\text{kpc}} \right)^2 \left(\frac{\text{eV}}{h\nu_s} \frac{\nu_s F_{\nu_s}}{\text{eV cm}^{-2} \text{s}^{-1}} \right) \text{cm}^{-3}, \quad (8)$$

where $\nu_s F_{\nu_s}$ denotes the ADAF energy flux whose value lies around $10^{-12} \text{TeV cm}^{-2} \text{s}^{-1} = \text{eV cm}^{-2} \text{s}^{-1}$ at distance $d = 10 \text{ kpc}$; the ADAF spectrum peaks at $h\nu_s \approx$

a few eV (thin four curves on the left in fig. 4). We evaluate the ADAF luminosity (in near-IR energies) with $L_s \approx 4\pi d^2 \nu_s F_{\nu_s}$, where $d = 10$ kpc. To compute n_s , we assume that the photon density is uniform within $r = 10r_g$, a typical radius in which the equatorial ADAF is confined vertically by the magnetic pressure [McKinney et al. (2012)].

The electrons Lorentz factors are limited above 10^6 [Hirotani et al. (2018)]. Thus, the Klein-Nishina cross section becomes $\sigma_{\text{IC}} \approx 0.2\sigma_{\text{T}}$, where σ_{T} denotes the Thomson cross section. Thus, the mean-free path for the IC scatterings, $\lambda_{\text{IC}} = 1/(n_s\sigma_{\text{IC}})$, becomes

$$\frac{\lambda_{\text{IC}}}{r_g} \approx 4.0 \times 10^{-2} M_1 \left(\frac{10r_g}{r} \frac{d}{10\text{kpc}} \right)^{-2} \left(\frac{\text{eV}}{h\nu_s} \frac{\nu_s F_{\nu_s}}{\text{eV cm}^{-2} \text{s}^{-1}} \right)^{-1} \left(\frac{\sigma_{\text{IC}}}{\sigma_{\text{T}}} \right)^{-1}, \quad (9)$$

The pair-production cross section becomes slightly below $0.2\sigma_{\text{T}}$ for the collisions of TeV and eV photons with moderate angles. Thus, the sum of the IC and pair-production mean-free paths becomes

$$\frac{\lambda_{\text{IC}} + \lambda_{\text{pp}}}{r_g} \approx 2 \frac{\lambda_{\text{IC}}}{r_g} \approx 0.08 M_1 \left(\frac{\text{eV}}{h\nu_s} \frac{\nu_s F_{\nu_s}}{\text{eV cm}^{-2} \text{s}^{-1}} \right)^{-1}, \quad (10)$$

Note that the Klein-Nishina and the pair-production cross sections are exactly computed in the numerical analysis, taking account of the photon specific intensity and the particle distribution functions at each point. Electrons are accelerated by E_{\parallel} and attain the terminal Lorentz factor, $\gamma \sim 10^6$, after running the distance

$$\lambda_{\text{acc}} = \frac{\gamma m_e c^2}{e E_{\parallel}} = 1.7 \times 10^5 \left(\frac{|E_{\parallel}|}{10^4 \text{ statvolt cm}^{-1}} \right)^{-1} \frac{\gamma}{10^6}, \quad (11)$$

which is less than r_g .

We find that the gap becomes most luminous when

$$\lambda_{\text{IC}} + \lambda_{\text{pp}} + \lambda_{\text{acc}} \approx \lambda_{\text{IC}} + \lambda_{\text{pp}} \approx r_g = 1.5 \times 10^6 M_1 \text{cm}. \quad (12)$$

It follows from equation (10) that $\lambda_{\text{IC}} + \lambda_{\text{pp}} \approx 0.26r_g$ (or $\approx 0.40r_g$) is realized when $\dot{m} \approx 10^{-4}$ (or $\approx 6 \times 10^{-5}$), which gives $h\nu_s \approx \text{eV}$ and $\nu_s F_{\nu_s} \approx 0.3$ (or ≈ 0.2) $\text{eV cm}^{-2} \text{s}^{-1}$. It might appear that $\lambda_{\text{IC}} + \lambda_{\text{pp}} \approx r_g$ holds if $\dot{m} \ll 10^{-4}$. However, in this case, the gap width rapidly increases to diverge; that is, there exist no stationary solutions, (fig. 8 of [Hirotani & Pu (2016b)]). Because of the simplification adopted around equations (8)–(12), we could not obtain $\lambda_{\text{IC}} + \lambda_{\text{pp}} \approx r_g$ in this simplistic argument in a consistent manner with the numerical results of E_{\parallel} , γ , and the gamma-ray spectrum. Nevertheless, we can analytically conclude that the gap longitudinal width becomes comparable to the horizon radius and its luminosity maximizes when $\dot{m} \approx 10^{-4}$ for stellar-mass BHs.

To further analytically estimate E_{\parallel} , Lorentz factors, γ -ray energies, and so on without invoking on the numerical results, we have to perform the similar computations as described in § 2 of [Hirotani (2013)] for rotation-powered

pulsars. In this case, we would have to replace the curvature process with the IC process, the neutron-star surface X-ray field with the ADAF IR field, the neutron-star magnetic field with that created/supported by the ADAF, and the light-cylinder radius with r_g (to compute the spatial gradient of $\rho_{G,J}$). For pulsars, the pair-production optical depth, τ_{pp} , is much less than unity for the out-going, curvature GeV photons, which tail-on collide with the neutron-star surface X-rays. However, for BHs, $\tau_{pp} \sim 1$ holds for the IC TeV photons whose collision angles are typically 0.5–1.0 rad with the ADAF-emitted near-IR photons. It is noteworthy that the gap longitudinal width becomes approximately $\lambda_{IC} + \lambda_{pp} + \lambda_{acc}$, because $\tau_{pp} \sim 1$ holds for BH gaps. It is, however, out of the scope of the present paper to inquire the further details of this analytical method.

7 Discussion

Let us compare the related gamma-ray emission scenarios. In the protostellar jet scenario [Bosch-Ramon et al. (2010)], electrons and protons are accelerated at the termination shocks when the jets from massive protostars interact with the surrounding dense molecular clouds. Thus, the size of the emission region becomes comparable to the jet transverse thickness at the shock. In the hadronic cosmic ray scenario [Ginzburg & Syrovatskii (1964), Blandford & Eichler (1987)], protons and helium nuclei are accelerated in the supernova shock fronts and propagate into dense molecular clouds, resulting in a single power-law photon spectrum in 0.001 – 100 TeV through neutral pion decays. The size becomes comparable to the core of a dense molecular cloud. In the leptonic cosmic ray scenario [Aharonian et al. (1997), van der Swaluw et al. (2001), Hillas et al. (1998)], electrons are accelerated at pulsar wind nebulae or shell-type supernova remnants, and radiate gamma-rays via IC process and radio/X-rays via synchrotron process. Since the cosmic microwave background radiation provides the main soft photon field in the interstellar medium, the size may be comparable to the plerions, whose size increases with the pulsar age. In the black-hole lepton accelerator scenario [Beskin et al. (1992), Hirotsu & Okamoto (1998), Neronov & Aharonian (2007), Levinson (2011), Globus & Levinson (2014), Broderick & Tchekhovskoy (2015), Hirotsu et al. (2017), Levinson & Segev (2017)], emission size does not exceed $10r_g$. Noting that the angular resolution of the CTA is about five times better than the current IACTs, we propose to discriminate the present black-hole lepton accelerator scenario from other scenarios by comparing the gamma-ray image and spectral properties. Namely, if a VHE source has a point-like morphology like HESS J1800-2400C in a gaseous cloud (section S1), and has two spectral peaks in 0.01 – 3 GeV and 0.01 – 1 TeV, but shows (synchrotron) power-law component in neither radio nor X-ray wavelengths, we consider that the present scenario accounts for its emission mechanism.

References

- Aharonian et al. (1997). F. A. Aharonian, A. M. Atoyan, T. Kifune, *Mon. Not. R. Astron. Soc.*, **291**, 162 (1997).
- Beskin et al. (1992). V. S. Beskin, Ya. N. Istomin, V. Paredes, *Sov. Astron.*, **36(6)**, 642 (1992).
- Black & Fazio (1973). J. H. Black, G. G. Fazio, *ApJ*, **185**, L7-11 (1973)
- Blandford & Znajek (1977). R. D. Blandford, R. L. Znajek, *Mon. Not. R. Astron. Soc.*, **179**, 433 (1977).
- Blandford & Eichler (1987). R. D. Blandford, D. Eichler, *Phys. Rep.*, **154**, 1 (1987).
- Bondi & Hoyle (1944). H. Bondi, F. Hoyle, *Mon. Not. R. Astron. Soc.*, **104**, 273 (1944).
- Broderick & Tchekhovskoy (2015). A. E. Broderick, A. Tchekhovskoy, *809*, **97**, (2015).
- Bosch-Ramon et al. (2010). Bosch-Ramon, G. E. Romero, A. T. Araudo, J. M. Paredes, *Astron. Astroph.*, **511**, 8 (2010).
- Boyer & Lindquist (1967). R. H. Boyer, R. W. Lindquist, *J. Math. Phys.* **265**, 281 (1967).
- Cheng et al. (1986a). K. S. Cheng, C. Ho, M. Ruderman, *Astroph. J.* **300**, 500 (1986a).
- Cheng et al. (2001). K. S. Cheng, M. Ruderman, L. Zhang, *Astroph. J.* **537**, 964 (2000).
- Ciang & Romani (1992). J. Chiang, R. W. Romani, *Astroph. J.* **400**, 629 (1992).
- Corral-Santana et al. (2016). J. M. Corral-Santana, J. Casares, T. Munoz-Daias, F. E. Bauer, I. G. Martinez-Pairs, D. M. Russel, *Astron. Astroph.*, **587**, (2016).
- de Wilt et al. (2017). P. de Wilt, G. Rowell, A. J. Walsh, M. Burton, J. Rathborne, Y. Fukui, A. Kawamura, F. Aharonian, *MNRAS* **468**, 2093-2113 (2017)
- Ginzburg & Syrovatskii (1964). V. L. Ginzburg, S. I. Syrovatskii, *18. The Origin of Cosmic Rays* (New York; Macmillan), (1964)
- Globus & Levinson (2014). N. Globus, A. Levinson, *Astroph. J.*, **796**, 26 (2014).
- Goldreich & Julian (1969). P. Goldreich, W. H. Julian, *ApJ* **157**, 869 (1969).
- Hillas et al. (1998). A. M. Hillas, C. W. Akerlof, S. D. Biller, J. H. Buckley, D. A. Carter-Lewis, M. Catanese, M. F. Cawley, D. J. Fegan, et al. *Astroph. J.*, **503**, 744 (1998).
- Hirotani & Okamoto (1998). K. Hirotani, I. Okamoto, *Astroph. J.*, **497**, 563 (1998).
- Hirotani & Shibata (1999). K. Hirotani, S. Shibata *MNRAS* **308**, 54 (1999).
- Hirotani (2006). K. Hirotani, *Mod. Phys. Lett. A (Brief Review)*, **21**, 1319 (2006).
- Hirotani (2013). K. Hirotani *Astroph. J.*, **766**, 98 (2013).
- Hirotani & Pu (2016b). K. Hirotani, H.-Y. Pu, *Astroph. J.*, **818**, 50 (2016a).
- Hirotani et al. (2016a). K. Hirotani et al., *Astroph. J.*, **833**, 142, (2016b)
- Hirotani et al. (2017). K. Hirotani, H.-Y. Pu, L. C.-C. Lin, A. K. H. Kong, S. Matsushita, K. Asada, H.-K. Chang, P.-H. T. Tam, *ApJ* **845**, 77 (2017).
- Hirotani et al. (2018). K. Hirotani, H.-Y. Pu, S. Outmani, H. Huang, D. Kim, Y. Song, S. Matsushita, A. K. H. Kong, *submitted to ApJ* (2018).
- Ichimaru (1979). S. Ichimaru, *Astroph. J.*, **214**, 840 (1979).
- Issa & Wolfendale (1981). M. R. Issa, A. W. Wolfendale, *Nature* **292**, 430-433 (1981)
- Kerr (1963). R. P. Kerr, *PRP* **11**, 237 (1963).
- Komissarov & McKinney (2007). S. S. Komissarov, J. C. McKinney, *Mon. Not. R. Astron. Soc.*, **377**, L49 (2007).
- Levinson (2011). A. Levinson, F. Rieger, *Astroph. J.*, **730**, 123 (2011).
- Levinson & Segev (2017). A. Levinson, N. Segev, *PRD* **96**, id.123006 (2017).
- Mahadevan (1997). R. Mahadevan, *Astroph. J.*, **477**, 585 (1997).
- Mestel (1971). L. Mestel, *Nature* **233**, 149 (1971).
- Narayan (1994). R. Narayan, I. Yi, *Astroph. J.*, **428**, L13 (1994).
- McKinney et al. (2012). J. C. McKinney, A. Tchekhovskoy, R. R. Blandford, *MNRAS*, **423**, 3083 (2012).
- Neronov & Aharonian (2007). A. Neronov, F. A. Aharonian, *Astroph. J.*, **671**, 85 (2007).
- Romani (1996). R. Romani, *Astroph. J.*, **470**, 469 (1996).
- Song et al. (2017). Y. Song, H.-Y. Pu, K. Hirotani, S. Matsushita, A. K. H. Kong, H.-K. Chang, *Mon. Not. R. Astron. Soc.*, **471**, L135 (2017).
- Tchekhovskoy et al. (2010). A. Tchekhovskoy, R. Narayan, J. C. McKinney, *Astroph. J.*, **711**, 50 (2010).
- Tetarenko et al. (2016). B. E. Tetarenko, G. R. Sivakoff, C. O. Heinke, J. C. Glandstone, *Asoroph. J. Suppl.*, **222**, 15 (2016).
- van der Swaluw et al. (2001). E. van der Swaluw, A. Achterberg, Y. A. Gallant, G. Toth, *Astron. Astroph.*, **380**, 309 (2001).
- Wilhelmi (2009). E. De Ona Wilhelmi, *AIP Conf. Ser.* **1112**, p. 16-22 (2009)